CDF/ANAL/BOTTOM/CDFR/10385
Version 1.0 – January 25, 2011

Determination of Polarization Parameters in Decays of Heavy Quarkonium

Matthew Jones

Purdue University

1 Introduction

In the *Allegory of the Cave*[1], Plato describes an unfortunate group of people whose only information about the world around them is obtained by viewing the shadows that objects cast on the wall of a cave. Because they have remained in this state for so long, they regard the shadows as reality itself and are not fully aware of the nature of the objects that cast the shadows. Although it would be straight forward for them to measure the length of the shadow of, for example, a stick, it would be difficult for them to reach a consensus on the true length of the stick if its orientation with respect to the wall of the cave were unknown.

This allegory closely approximates the current status of experiments that have attempted to obtain information about the polarization of J/ψ and Υ mesons produced at hadron colliders. So far, experiments have only reported measurements[2, 3] of the angular distribution of the $\mu^+\mu^-$ in the final state, projected onto the momentum vector of the heavy meson. These measurements are not in direct agreement, but are also not contradictory given that different experiments apply widely different acceptance corrections to different samples of events collected over different ranges of kinematic variables.

This note describes a fitting procedure that determines the three parameters that completely characterize the production polarization of vector mesons. If we act fast, it could be applied to provide the first experimental measurements of these parameters in a form that could be directly compared with other experiments, in particular those at the LHC.

2 Angular Distributions

In a specified reference frame, the angular distribution of the positive muon in the decay $\psi \to \mu^+\mu-$ can be written

$$\begin{aligned}\frac{d\Gamma}{d\Omega} \quad \propto \quad & 1 + \lambda_\theta \cos^2\theta + \lambda_\varphi \sin^2\theta \cos 2\varphi + \lambda_{\theta\varphi} \sin 2\theta \cos\varphi + \\ & \lambda_\varphi^\perp \sin^2\theta \sin 2\varphi + \lambda_{\theta\varphi}^\perp \sin 2\theta \sin\varphi \end{aligned} \tag{1}$$

however the coefficients $\lambda_\varphi^\perp$ and $\lambda_{\theta\varphi}^\perp$ are not directly observable due to symmetries of the angular distribution arising from parity invariance of the initial state. Thus, there are three observable parameters that can be determined from the angular information in vector meson decays. Intuitively,

this number of degrees of freedom can deduced by considering two angles to describe the orientation of the spin vector of a vector meson, and one parameter to describe the relative fraction of the spin density that is in the longitudinal or transverse state.

The difficulty that arises in fitting this distribution to experimental data, is that it is significantly modified by detector acceptance. This was addressed in previous analysis by forcing $\lambda_\varphi = \lambda_{\theta\varphi} = 0$, and calculating the observed distributions of $\cos^2\theta$ that arise from the underlying distributions $d\Gamma/d\Omega \propto 1 \pm \cos^2\theta$ being subjected to a Monte Carlo simulation of the trigger and detector acceptance. The observed distribution of $\cos^2\theta$ is then fit to a linear combination of these pure longitudinal and transverse templates, from which the coefficient λ_θ can be obtained. Unfortunately, this procedure does not generalize easily to higher dimensions.

The approach used in this analysis is to simulate the response of the detector acceptance to an un-polarized angular distribution, and re-weight the two-dimensional distribution of (θ, φ) so as to calculate the expected angular distribution, given polarization parameters λ_θ, λ_φ and $\lambda_{\theta\varphi}$. For realistic p_T and η requirements on the muons in the final state, the acceptance is a strong function of their invariant mass which must be taken into account when subtracting the effect of the combinatorial background from the heavy quarkonium signal polarization. The polarization of the background is assumed to vary continuously with invariant mass but is constrained by the sidebands.

The fit is performed by maximizing a log-likelihood function constructed as follows. For a particular range of kinematic variables, like p_T and η, the sample is divided into N bins based on invariant mass. The bins are chosen so that the signal of interest is contained in one bin while others are dominated by background. Within each bin of invariant mass, a two-dimensional histogram is filled with the angular variables (θ, φ) such that in bin i of this distribution, we observe x_i events. Furthermore, vector meson decays are generated uniformly in p_T and rapidity over this range and the kinematics of the decay to the $\mu^+\mu^-$ final state is calculated assuming an isotropic decay distribution. The final state is then required to satisfy the same restrictions on p_T and η imposed by the trigger used to collect the signal candidates and the un-polarized acceptance distributions in (θ, φ) are filled. In practice, we keep track of the number, M_i, of simulated signal events generated in (θ, φ) bin i and the number of events, m_i, in that bin that satisfied the acceptance criteria. An un-polarized background sample is also generated with a uniform distribution of invariant mass and after imposing acceptance restrictions, the distribution of (θ, φ) is recorded. For these distributions the number of events generated that populate bin i is denoted N_i and the number accepted is n_i.

2.1 Background only fit

The derivations of the expressions presented in this section are described in more detail elsewhere[4], but the main results are motivated as follows. The likelihood function for a given mass bin, j, containing only background is constructed thus:

$$\mathcal{L}^{(j)}_{bkg} = \prod_i p(w_i(\vec{\lambda}_{bkg})Z/\Delta_i, x_i, M_i, m_i) \tag{2}$$

where $p(Z, x, M, m)$ is the probability density function for observing x events to satisfy the acceptance criteria out of Z events present given that the Monte Carlo calculation found m out of M events generated to satisfy the acceptance criteria. This probability density is constructed in such a way that the estimator of the acceptance $\mathcal{A} = m/M$ is integrated over, assuming a binomial probability distribution for m with unknown parameter $\mathcal{A}$. It is reasonable to approximate the Poisson probability distribution for x_i with a binomial distribution, in which case we can write

$$p(Z, x, M, m) = \left[\frac{(M+1)!(x+m)!}{x!m!(M-m)!}\right] \frac{Z!}{(Z-x)!} \frac{(Z+M-x-m)!}{(Z+M+1)!}. \tag{3}$$

Except for the approximation of the Poisson distribution by the binomial distribution, this expression is exact and applies even when bins in either distribution contain small numbers of entries. This

is important because the boundaries of the accepted region in (θ, φ) consist of many such bins and biases in the fit will arise if only bins with statistics greater than, say, 5 or 10, are considered in the fit. In Equation 2, the yield of background events, Z, is weighted by the factors $w_i(\vec{\lambda})$ calculated using Equation 1, with parameters $\vec{\lambda} = (\lambda_\theta, \lambda_\varphi, \lambda_{\theta\varphi})$ to scale the number of events present in the entire angular range by the number expected to fall within bin i. For an isotropic decay, $w_i(\vec{\lambda}) \equiv 1$ and the expected number of events in bin i would just be Z/Δ_i, where $1/\Delta_i$ is the fraction the un-polarized distribution expected to be contained in bin i. In the case of N_θ and N_φ bins of equal size, there are a total of $N_\theta N_\varphi$ bins and so $\Delta_i = N_\theta N_\varphi$.

2.2 Signal+background fit

When a region j of invariant mass contains both signal and background events, the likelihood function is constructed as follows:

$$\mathcal{L}^{(j)}_{sig+bkg} = \prod_i q(w_i(\vec{\lambda}_{sig})Y/\Delta_i, w_i(\vec{\lambda}_{bkg})Z/\Delta_i, x_i, M_i, m_i, N_i, n_i) \tag{4}$$

where $q(Y, Z, x, M, m, N, n)$ is the probability of observing x events to satisfy the acceptance requirements when Y signal and Z background events were present and where m out of M signal events and and n out of N background events in the Monte Carlo samples were accepted. In the case when $x < Z$, this probability distribution is

$$\begin{aligned} q(Y, Z, x, \ldots) &= \sum_{y=0}^{x} p(Y, y, M, m) q(Z, x-y, N, n) && (5) \\ &= \left[\frac{(M+1)!(N+1)!Z!(n+x)!(N+Z-n-x)!}{(N-n)!(M-m)!n!x!(Z+N+2)!(Z-x)!}\right] \times \\ &\qquad \frac{(M+Y-m)!}{(M+Y+1)!} F\left(\begin{array}{c} -x, -Y, m+1, N+Z-n-x+1 \\ -n-x, m-M-Y, Z-x+1 \end{array}; 1\right) && (6) \end{aligned}$$

and when $x \geq Z$ this is

$$\begin{aligned} q'(Y, Z, x, \ldots) &= \sum_{y=x-Z}^{x} p(Y, y, M, m) p(Z, x-y, N, n) && (7) \\ &= \left[\frac{(M+1)!(N+1)!(m+x-Z)!(Z+n)!}{n!m!(M-m)!(x-Z)!(Z+N+1)!}\right] \frac{Y!(Y+M+Z-m-x)!}{(M+Y+1)!(Y+Z-x)!} \times \\ &\qquad F\left(\begin{array}{c} -Z, x-Y-Z, m+x-Z+1, N-n+1 \\ -n-Z, x-Z+1, m+x-M-Y-Z \end{array}; 1\right). && (8) \end{aligned}$$

The are expressed in terms of the hypergeometric function,

$$F\left(\begin{array}{c} a_0, a_1, \cdots a_p \\ b_0, b_1, \cdots b_q \end{array}; z\right) = \sum_{k=0}^{\infty} \frac{(a_0)_k (a_1)_k \cdots (a_p)_k}{(b_0)_k (b_1)_k \cdots (b_q)_k} \frac{z^k}{k!} \tag{9}$$

in which $(a)_k$ is the Pocchammer symbol,

$$(a)_k = a(a+1)(a+2)\cdots(a+k-1). \tag{10}$$

The distributions are normalized such that

$$\sum_{x=0}^{Z-1} q(\ldots, x, \ldots) + \sum_{x=Z}^{Y} q'(\ldots, x, \ldots) = 1. \tag{11}$$

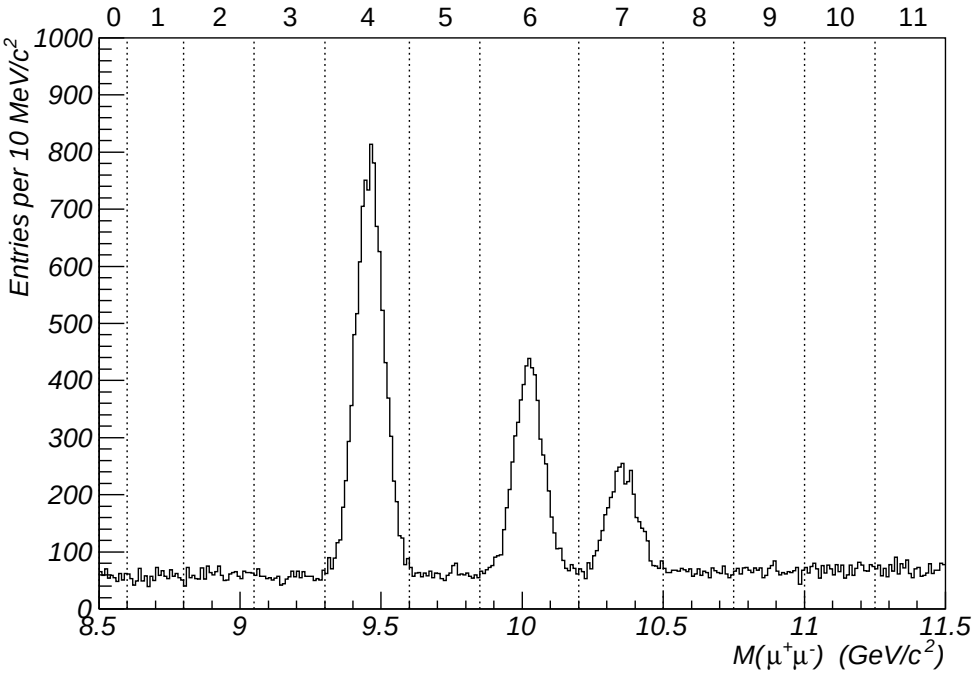

Figure 1: Invariant mass distribution of simulated $\Upsilon(nS)$ and background events. Vertical lines indicate the boundaries of the invariant mass bins used in the analysis.

It should be emphasized that similar likelihood functions could be constructed by means of other approximations, for example with estimates of the acceptance and its uncertainty in each bin, but these may not necessarily provide efficient and unbiased estimates of the signal yield when bins with small statistics are ignored in order to improve the quality of the approximation in the bins that remain.

3 Example Fits

To illustrate the behavior of the fit we analyze toy Monte Carlo samples of $\Upsilon(1S)$, $\Upsilon(2S)$ and $\Upsilon(3S)$ decays superimposed on combinatorial background. The signal samples are generated as Gaussian mass distributions with polarization in the Collins-Soper frame specified in terms of parameters $\vec{\lambda}_{nS}$. The background is uniformly distributed from 8.5 to 11.5 GeV/c^2 with polarization parameters, $\vec{\lambda}_{bkg}(m)$, that could vary linearly with invariant mass. The momentum range considered was $9.5 < p_T(\mu^+\mu^-) < 10.5$ GeV/c and the final state muons were required to satisfy $p_T > 4$ GeV/c and $|p_z/p_T| < 1$, which roughly approximates the kinematic and geometric acceptance of the detector.

The toy Monte Carlo sample consisted of $1S$, $2S$, and $3S$ signal events in the proportion 4:2:1, with mass splittings fixed to measured values and with their width set to 50 MeV/c^2. These signals and the level of simulated background is shown in Figure 1. In this figure, the background rises slightly at higher masses because it was generated with a uniform distribution, but the acceptance increases with invariant mass. Figure 2 illustrates how the background acceptance changes over the range of invariant masses considered. The background rate and the three background polarization parameters are treated in the fit as linear functions of the di-muon invariant mass and each signal is fit with independent yield and polarization parameters. Thus, there are 20 parameters in the

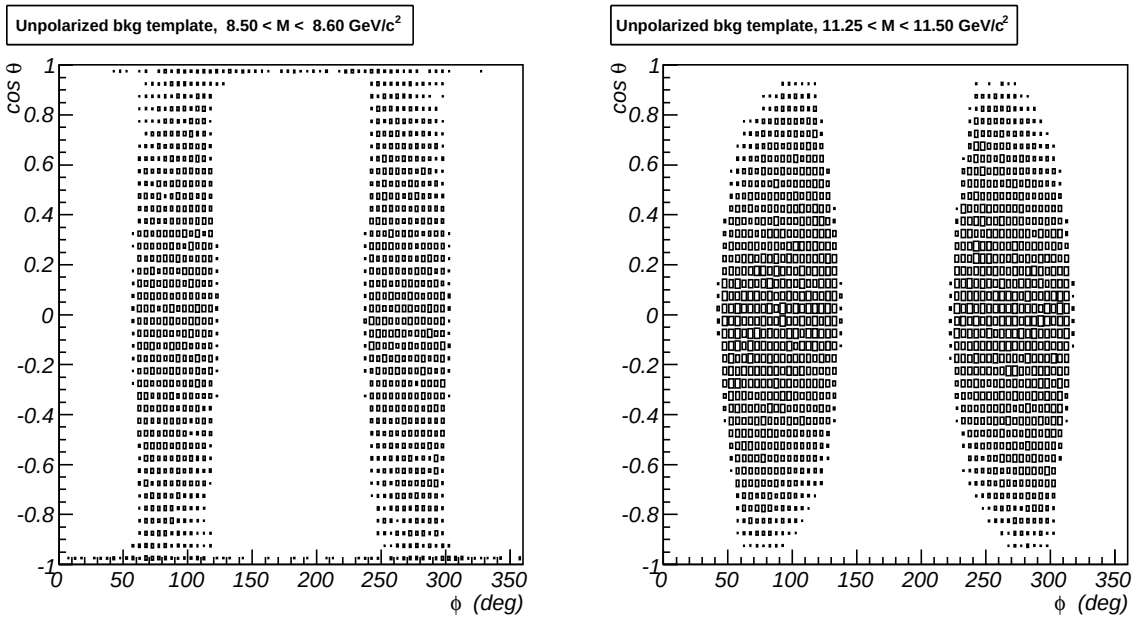

Figure 2: Angular distribution for un-polarized background events that pass the acceptance requirements for two different ranges of invariant mass.

fit. Signal samples used to calculate the acceptance each consisted of 500,000 events, while the background sample had 5×10^6 events. For $\langle p_T \rangle \sim 10$ GeV/c, the average acceptance is about 10%.

In this example, approximately 664 experiments were simulated in which there were 10^5, 5×10^4 and 2.5×10^4 events in the $\Upsilon(1S)$, $\Upsilon(2S)$ and $\Upsilon(3S)$ samples, respectively. Although only unpolarized Υ signals and background were generated, the polarization parameters were allowed to vary freely in the fit, as were the parameters describing the background rate and polarization parameters. Figure 3 shows the distribution of fitted yields and their pull distributions. At this time, while the yield estimates appear to be more or less unbiased, their uncertainties seem to be underestimated by about 50%. Figure 4 shows the distributions of the λ_θ parameter for the $1S$, $2S$ and $3S$ signals in the toy experiments. Although generated with $\lambda_\theta = 0$, the fit returns estimates for this polarization parameter that are biased towards slightly negative values, although the size of this bias is less than half the estimated uncertainty. The uncertainty estimates appear to be underestimated by about 20%.

To ensure that fit parameters are within the physical limits, the λ_φ parameter is calculated from a fit parameter x_2:

$$\lambda_\varphi = \frac{1}{2}(1 + \lambda_\theta)x_2 \tag{12}$$

where $x_2 \in (-1, 1)$. Figure 5 shows the distribution of the fitted values of x_2. Although generally unbiased, the uncertainty on x_2 appears to be underestimated by about 50%. Figure 6 shows the distribution of the fitted parameter $\lambda_{\theta\varphi}$, In this case the calculated uncertainty on $\lambda_{\theta\varphi}$ appears is to be underestimated by about 15%.

Figure 7 shows the two dimensional contours in $(\lambda_\theta, \lambda_\varphi)$ resulting from several toy experiments, with the same signal statistics as describe above but with the $\Upsilon(1S)$ state generated with different polarizations. Figure 8 shows a similar example, with fits to samples generated with $15 < p_T(\mu^+\mu^-) < 20$ GeV/c. The precision is better in this case because of the higher average acceptance, but also because a greater range of angles is selected by the trigger cuts.

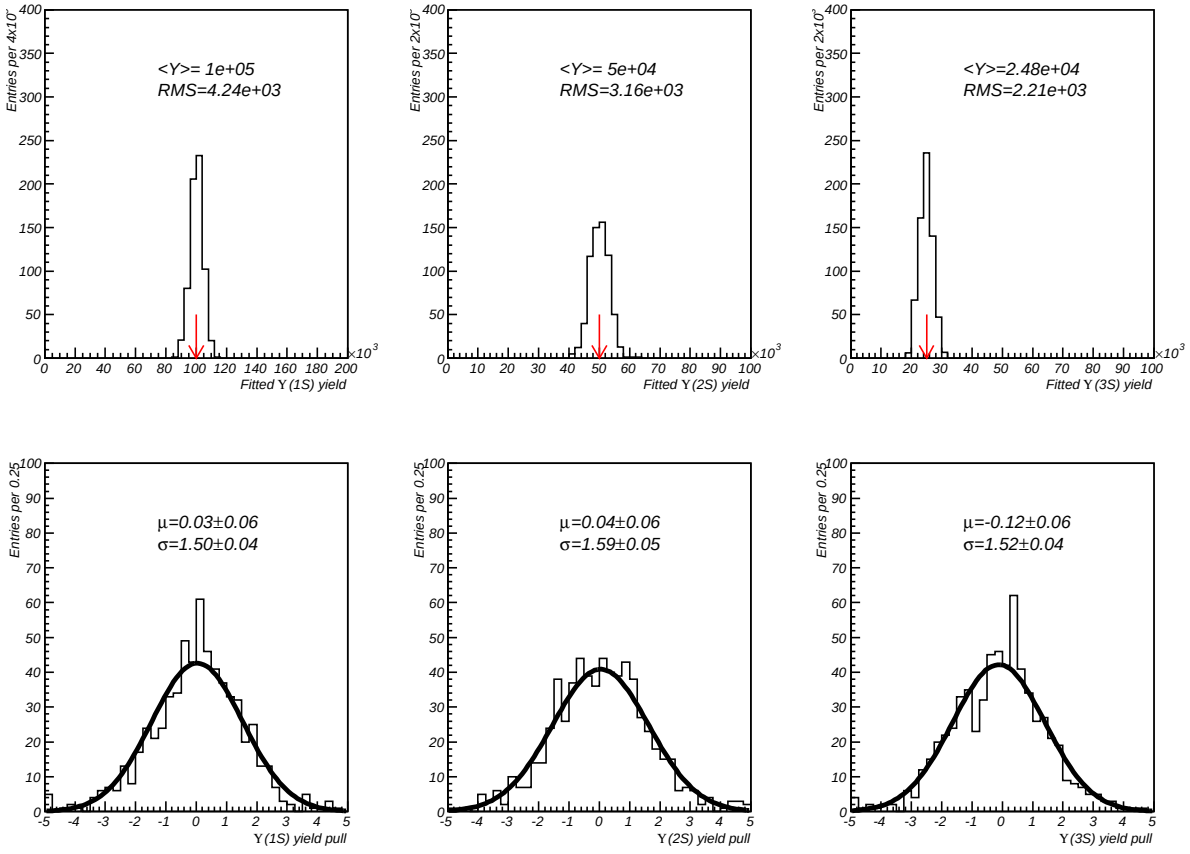

Figure 3: Fitted $\Upsilon(nS)$ yields for 664 toy Monte Carlo experiments generated and analyzed in the Collins-Soper frame. Arrows in the upper figures indicate the number of events generated.

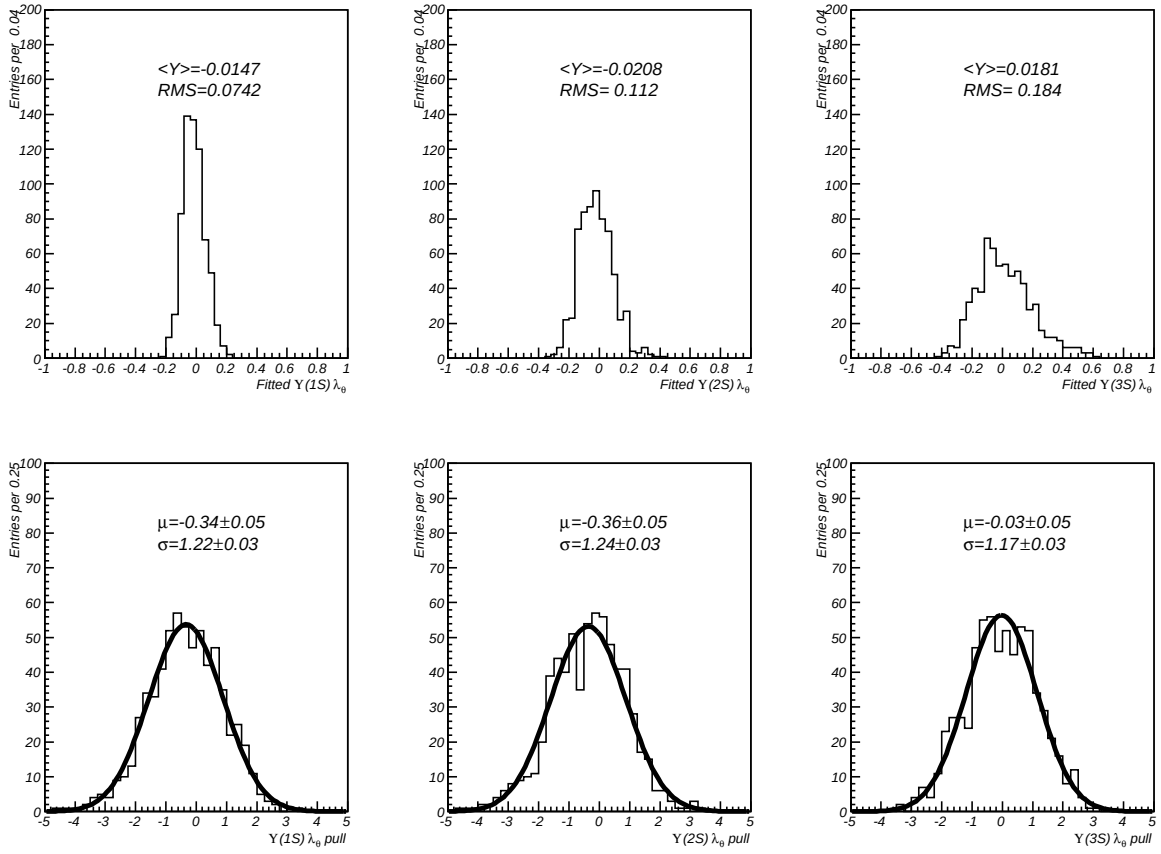

Figure 4: Fitted λ_θ parameters from 664 toy experiments with un-polarized $\Upsilon(nS)$ signal samples generated and analyzed in the Collins-Soper frame.

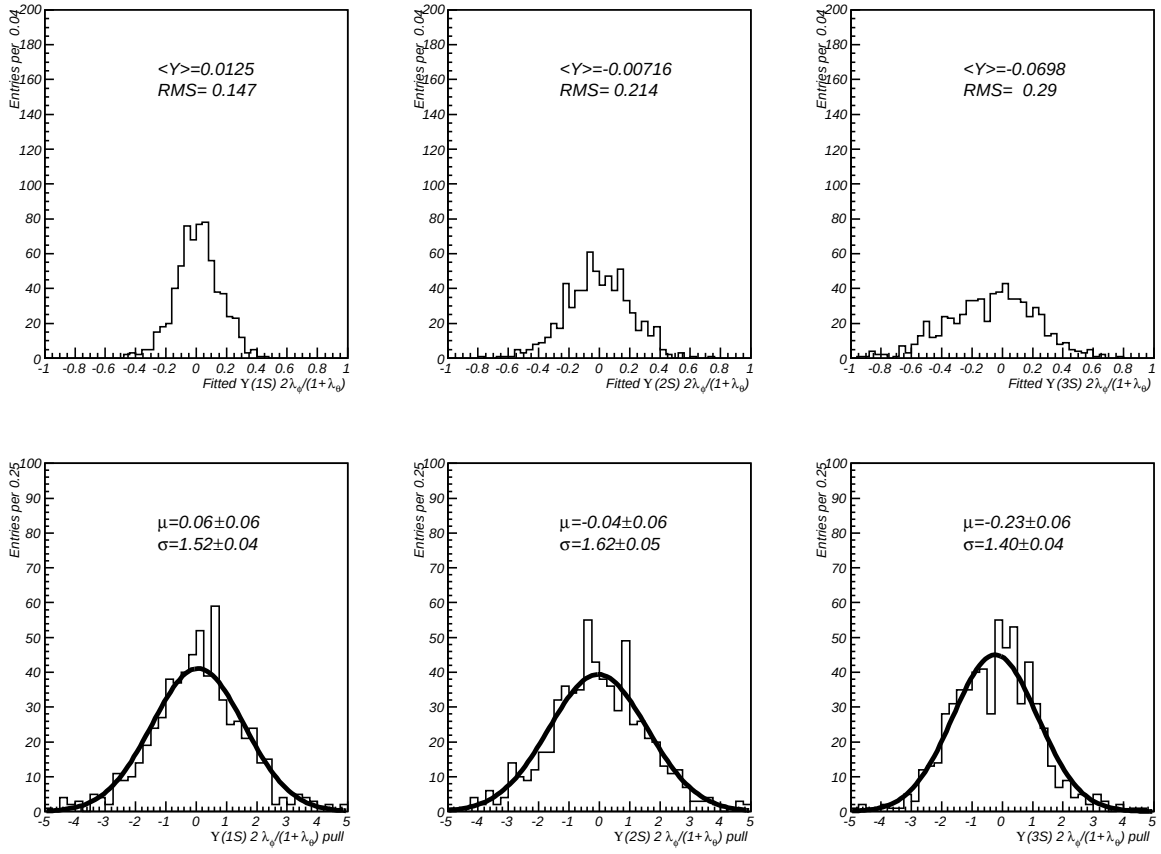

Figure 5: Fitted $x_2 = 2\lambda_\varphi/(1+\lambda_\theta)$ parameters from 664 toy experiments with un-polarized $\Upsilon(nS)$ signal samples, generated and analyzed in the Collins-Soper frame.

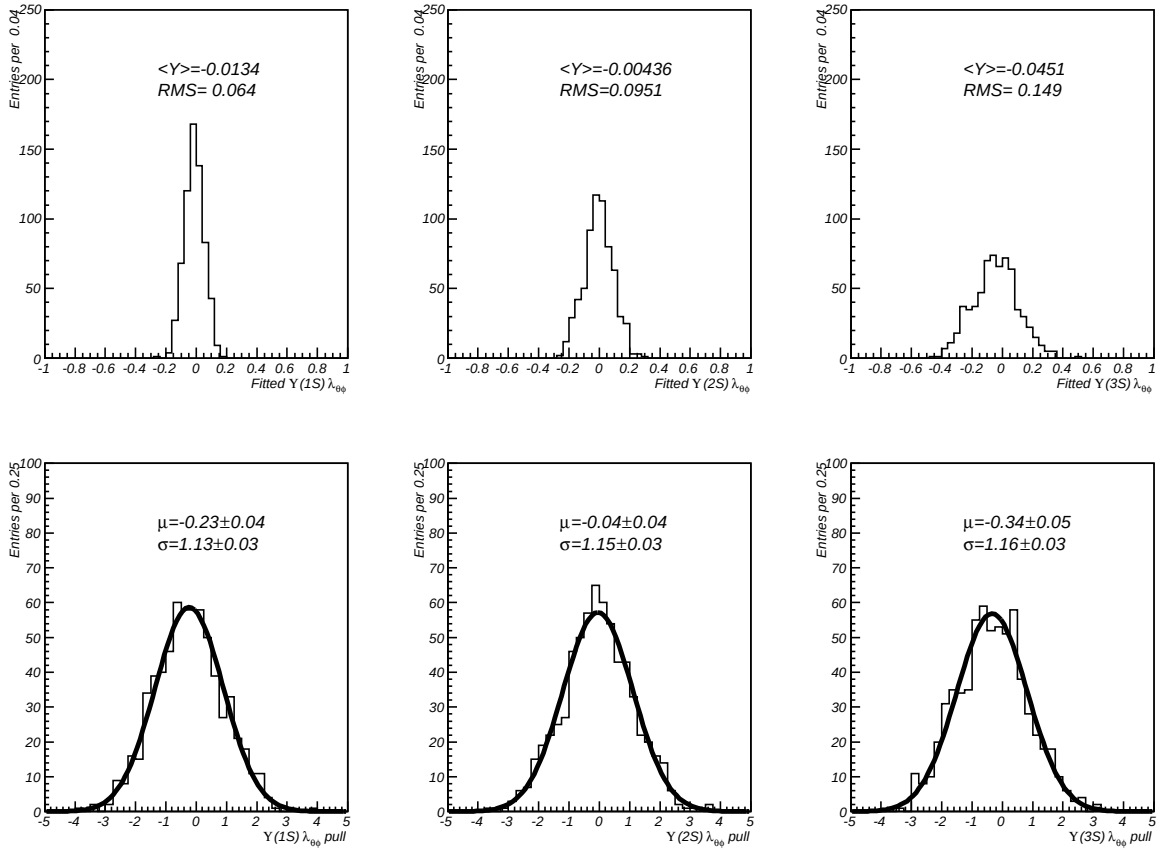

Figure 6: Fitted $\lambda_{\theta\varphi}$ parameters from 664 toy experiments with un-polarized $\Upsilon(nS)$ signal samples generated and analyzed in the Collins-Soper frame.

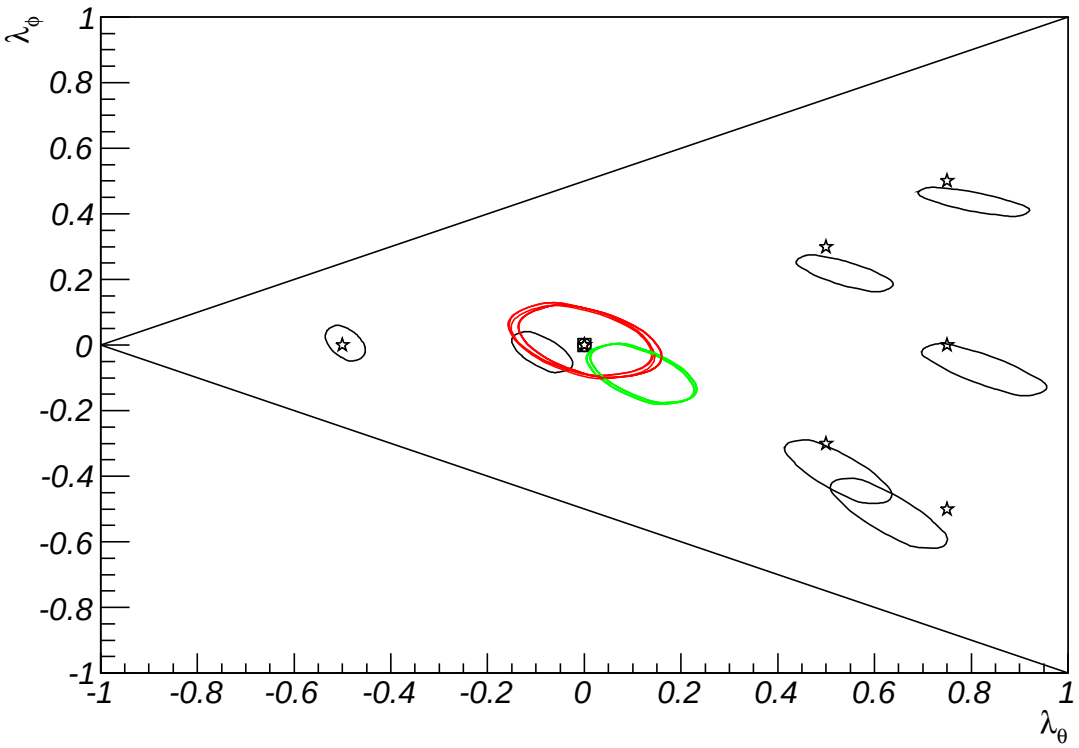

Figure 7: One-sigma contours for the λ_θ and λ_φ parameters for the $\Upsilon(nS)$ signals. The diagonal lines indicate the range of physically allowed parameters. The markers indicate the true polarization parameters used to generate the signal samples. Green and red contours are the one-sigma confidence intervals for the $\Upsilon(2S)$ and $\Upsilon(3S)$ polarization parameters. In this case, events were generated with $9.5 < p_T(\mu^+\mu^-) < 10.5$ GeV/c.

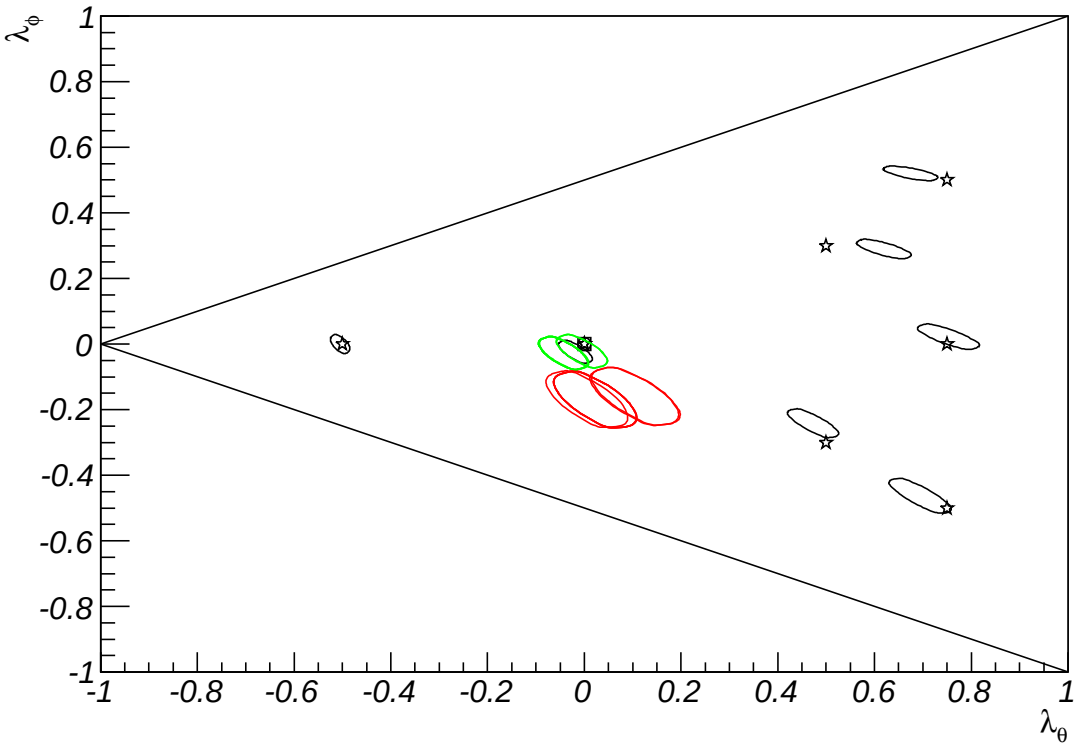

Figure 8: One-sigma contours for the λ_θ and λ_φ parameters for the $\Upsilon(nS)$ signals. The diagonal lines indicate the range of physically allowed parameters. The markers indicate the true polarization parameters used to generate the signal samples. Greed and red contours are the one-sigma confidence intervals for the $\Upsilon(2S)$ and $\Upsilon(3S)$ polarization parameters. These samples were generated with the same numbers of signal and background events as in the previous example, but with $15 < p_T(\mu^+\mu^-) < 20$ GeV/c.

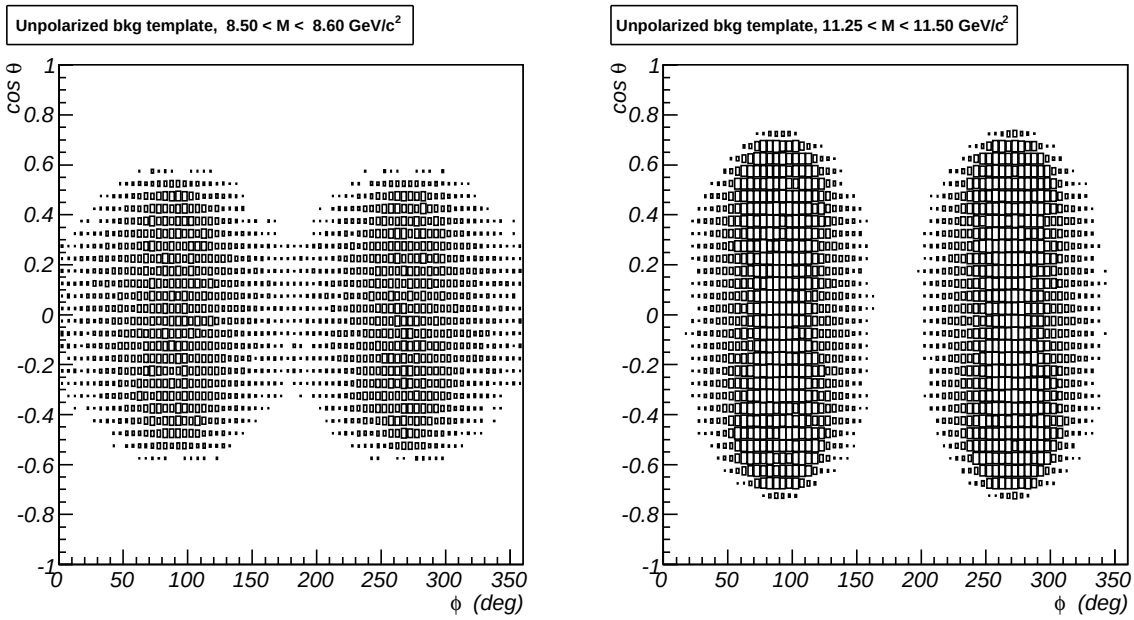

Figure 9: Background acceptance in the S-channel helicity frame.

4 Analysis in the S-channel Helicity Frame

4.1 Biases on yields and polarization estimates

The event generation described in the previous section was also performed in the S-channel helicity frame. Figure 9 shows the resulting resulting acceptance for the background at the two extremes of the mass distribution considered. This distribution is clearly quite different from the distribution obtained from analysis in the Collins-Soper frame. Figure 10 shows the fitted yields when analyzed in the S-channel helicity frame. When compared with Figure 3 it can be seen that the signal yields obtained from this analysis are more biased than when analyzed in the Collins-Soper frame. Similarly, Figures 11 to 13 indicate that although the polarization parameters are estimated with about the same precision as in the Collins-Soper frame, the biases are larger.

4.2 Analysis in multiple reference frames

We do not know, *a priori*, which reference frame exhibits the strongest polarization and we can analyze the same data in different reference frames. In general, the polarization parameters measured in one reference frame cannot be directly compared with those measured in another frame. Nevertheless, there are frame invariant quantities that can be calculated and compared in different frames. In particular, we consider the expression

$$\tilde{\lambda} = \frac{\lambda_\theta + 3\lambda_\varphi}{1 - \lambda_\varphi} \tag{13}$$

which will be $+1$ for transverse polarization in any reference frame and -1 for longitudinal polarization in any reference frame. To investigate this, two samples of events were generated in the S-channel helicity frame: one purely transverse polarized, with $\lambda_\theta = -1/3$ and $\lambda_\varphi = 1/3$ and the other purely longitudinally polarized with $\lambda_\theta = -1/3$ and $\lambda_\varphi = -1/3$.

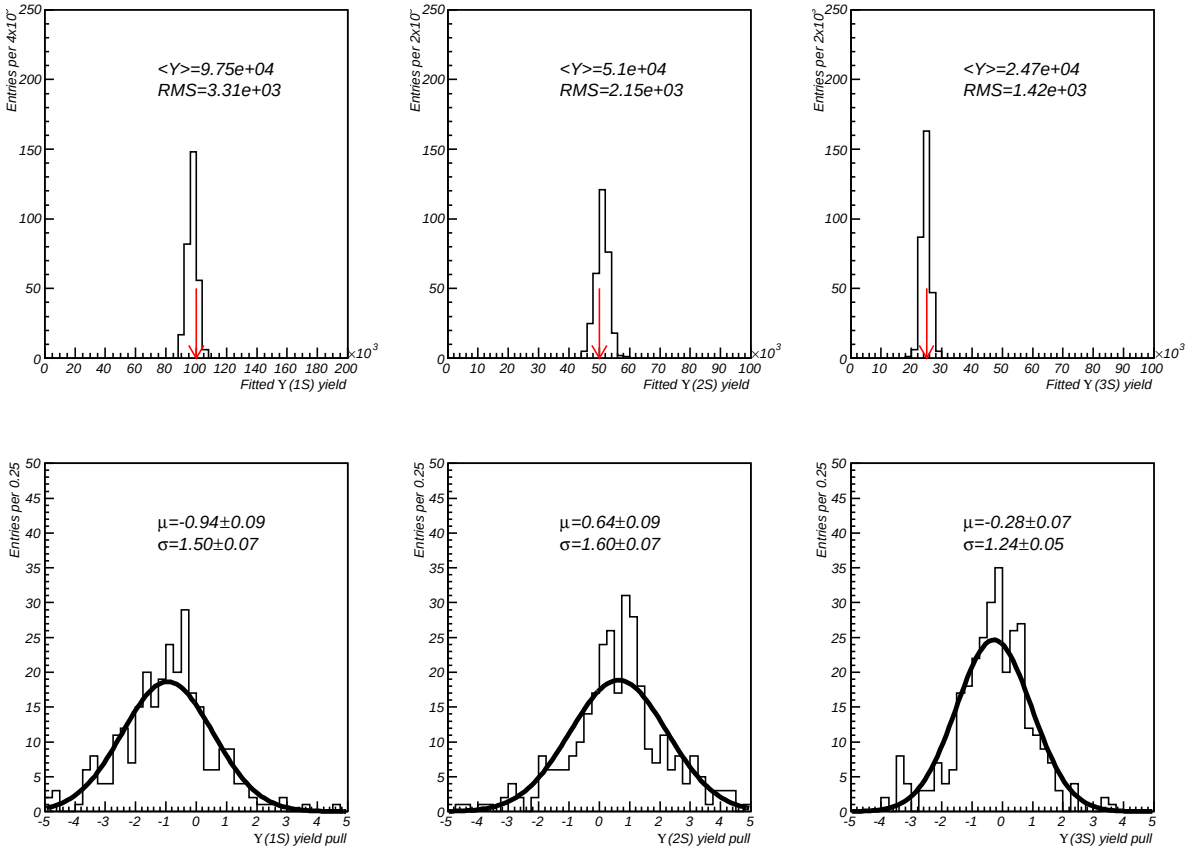

Figure 10: Distribution of fitted yields and their pull distributions when analyzed in the S-channel helicity frame.

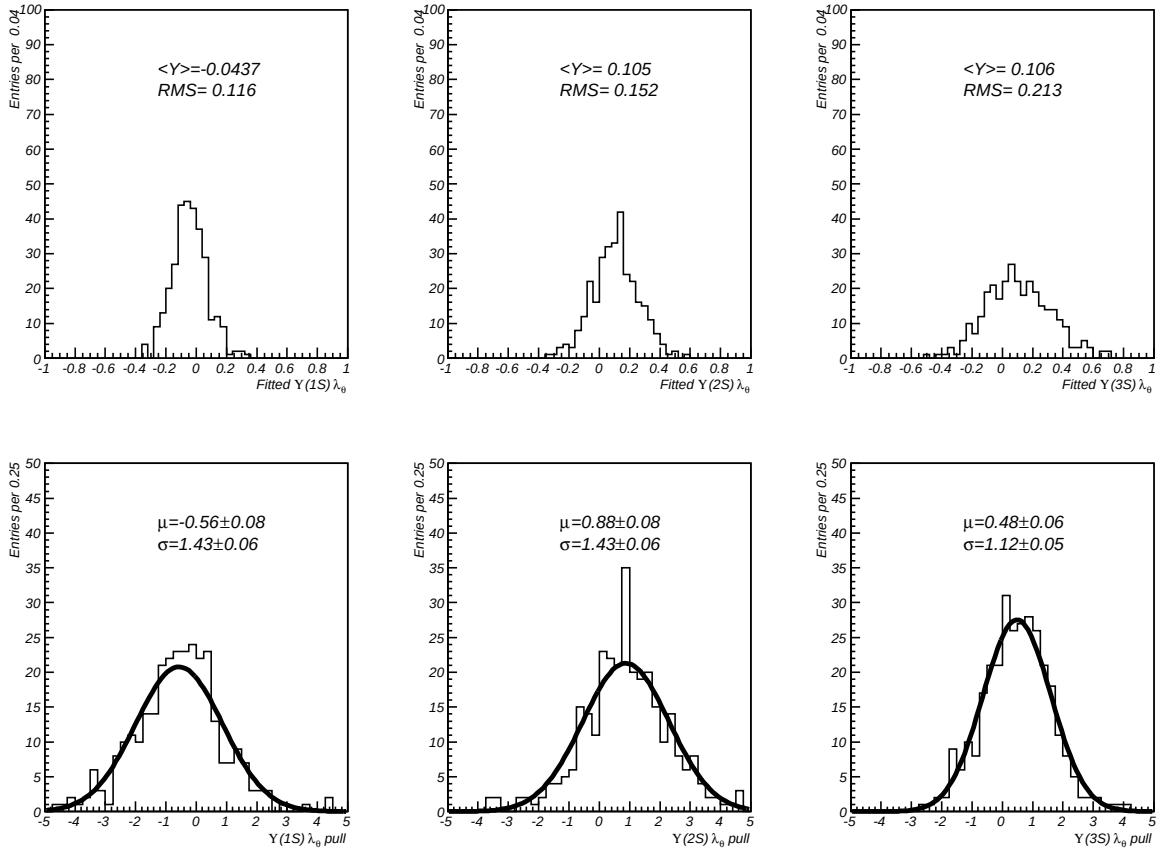

Figure 11: Fitted λ_θ parameters from toy experiments with un-polarized $\Upsilon(nS)$ signal samples generated and analyzed in the S-channel helicity frame.

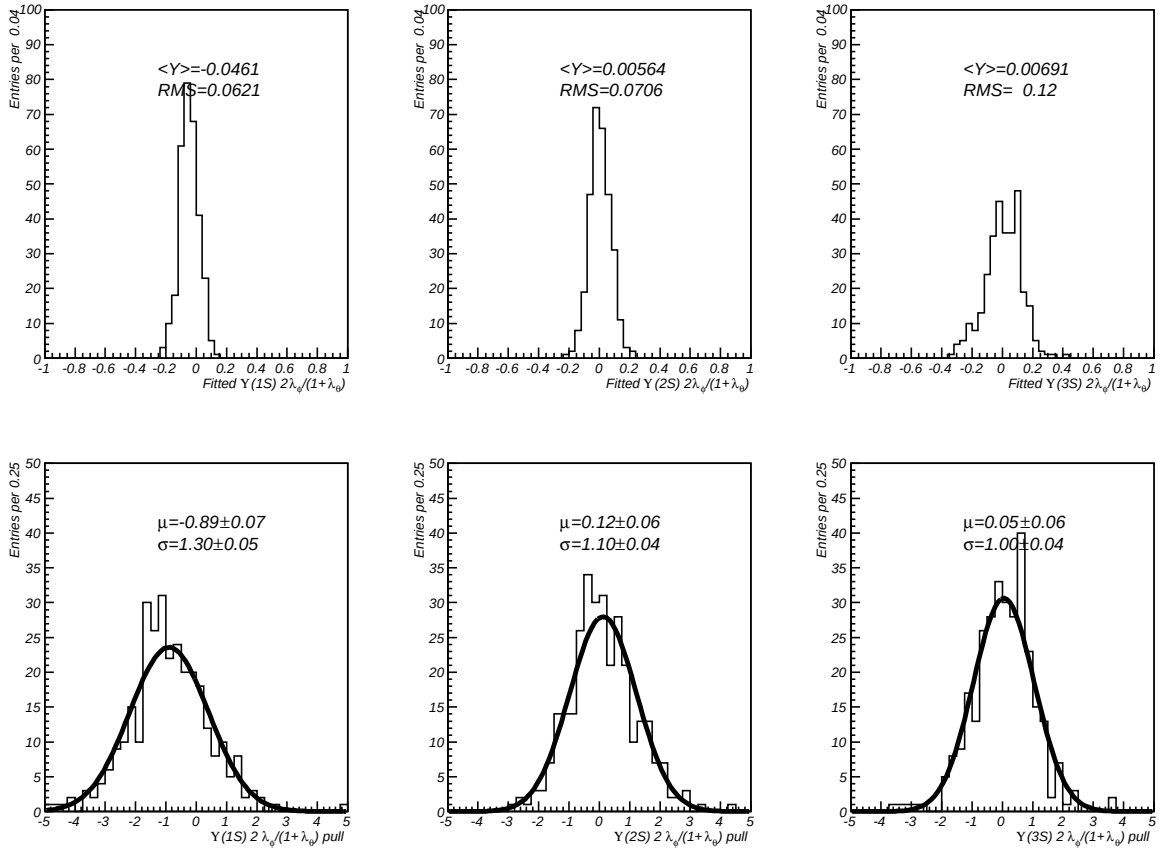

Figure 12: Fitted $x_2 = 2\lambda_\varphi/(1+\lambda_\theta)$ parameters from toy experiments with un-polarized $\Upsilon(nS)$ signal samples, generated and analyzed in the S-channel helicity frame.

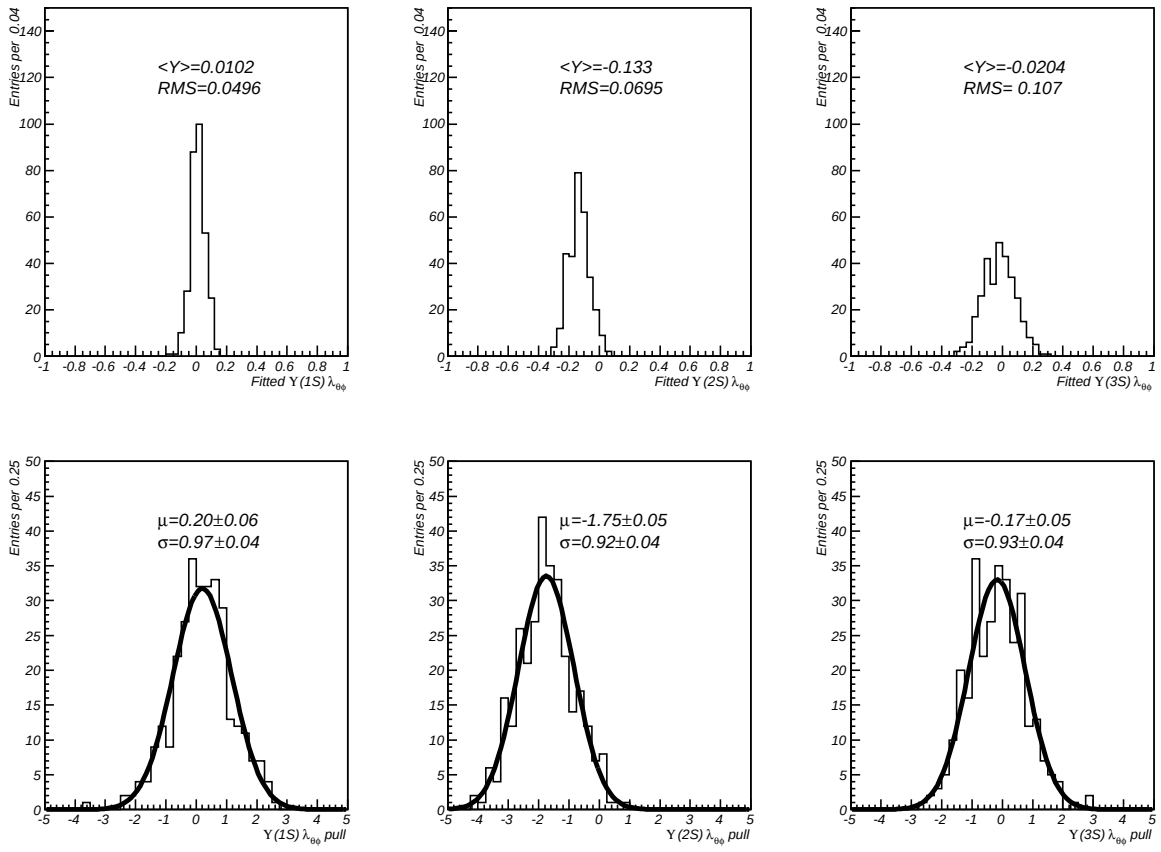

Figure 13: Fitted $\lambda_{\theta\varphi}$ parameters from toy experiments with un-polarized $\Upsilon(nS)$ signal samples generated and analyzed in the S-channel helicity frame.

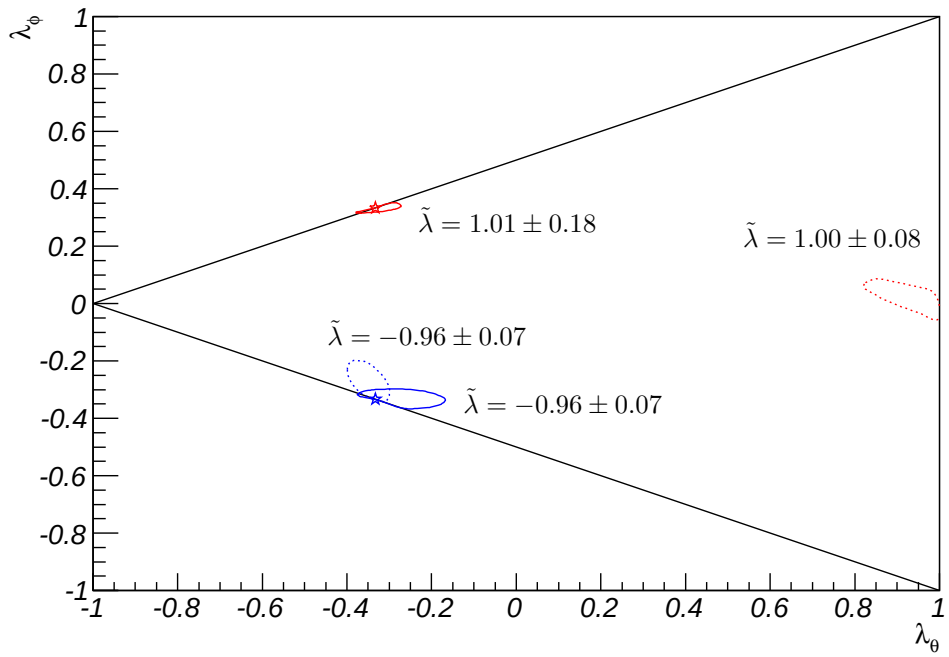

Figure 14: Polarization parameters for purely transverse and longitudinally polarized $\Upsilon(1S)$ states analyzed in the S-channel helicity (solid curves) and the Collins-Soper (dotted curves) frame. The parameters used to generate the states in the S-channel helicity frame are indicated by the markers. The measured values of the frame invariant quantity, $\tilde{\lambda}$, are indicated near each contour.

Each sample was analyzed in both the S-channel helicity frame, and the Collins-Soper frame, resulting in the $(\lambda_\theta, \lambda_\varphi)$ confidence intervals shown in Figure 14.

$p_T(\Upsilon)$ [GeV/c]	$N(1S)$	$N(2S)$	$N(3S)$	σ [MeV/c^2]	bkg [/MeV/c^2]
0-2	17072 ± 145	4532 ± 85	2113 ± 64	46.5 ± 0.4	33.2
2-4	76497 ± 320	19946 ± 196	9244 ± 149	48.1 ± 0.2	201.6
4-6	65490 ± 293	20439 ± 190	11173 ± 156	49.8 ± 0.2	180.1
6-8	38000 ± 221	11365 ± 139	5980 ± 112	49.3 ± 0.3	91.5
8-10	22780 ± 169	6998 ± 105	3980 ± 86	52.4 ± 0.3	41.9
10-12	13413 ± 129	4461 ± 81	2570 ± 66	54.9 ± 0.4	21.9
12-15	11216 ± 117	3895 ± 75	2353 ± 62	58.5 ± 0.5	16.7
15-20	7342 ± 95	2837 ± 63	1840 ± 543	63.7 ± 0.7	10.1
20-50	3183 ± 66	1461 ± 48	1039 ± 43	75.7 ± 1.4	6.2

Table 1: Approximate $\Upsilon(nS)$ signal yields, mass resolution and background level obtained from CMUP+CMU and CMUP+CMX triggers up to period 25. The background level is evaluated at $m(\mu^+\mu^-) = 8.5$ GeV/c^2 and therefore overestimates the background under the Υ signals.

5 Projections for CDF data

The statistics available in the upsilon sample, collected with CMUP+CMU and CMUP+CMX triggers, through period 25 is summarized in Table 1. Figure 15 shows an example of a fit to the di-muon mass distribution from which the yields shown in this table are determined. These events were selected by requiring that the CMUP muon have $p_T > 4$ GeV/c and the other have $p_T > 3$ GeV/c. The sample was further purified using the following criteria.

- $|z(\mu^+\mu^-)| < 60$ cm
- $|z_0(\mu^+) - z_0(\mu^-)| < 0.25$ cm
- $|d_0(\mu^\pm)| < 0.25$ cm
- $\mathcal{L}_{id}(\mu^\pm) > 0.05$
- $Iso_{\pi/2}(\mu^+\mu^-) > 0.15$

where $Iso_{\pi/2}$ is the ratio of the transverse momentum of the Υ candidate to the sum of the transverse momenta of the candidate and all other charged tracks in the same hemisphere as the candidate. These criteria were chosen after only a brief, and not particularly systematic study and are not expected to be optimal for any specific measurement. Nevertheless, they illustrate the levels of signal and background statistics that we have to work with in the current data. Requiring only the CMUP+CMU trigger path reduces the signal yields by 50-60%.

In order to make more realistic projections, a model of the geometric acceptance of CMUP, CMU and CMX muons was constructed. Figure 16 shows the ϕ_0 and $\cot\theta$ of reconstructed CMUP muons, selected to have $|z_0 - 25$ cm$| < 1$ cm, compared to the acceptance simulated using the model. Figure 17 shows the observed and simulated geometric acceptance of muons in CMX, which is restricted by both the coverage of the muon chambers and the COT. The fiducial region of CMU was approximated by a cylinder of radius 350 cm extending to $z = \pm 250$ cm. The luminous region was simulated using a Gaussian distribution centered at $z = 0$ with a width of 30 cm. The `UPSILON_CMUP_CMU` trigger was simulated by requiring one muon to be fiducial in CMUP with $p_T > 4$ GeV/c and the other muon to be fiducial in CMU with $p_T > 3$ GeV/c. If both muons were on the same side of the detector, they were required to be separated in azimuth by at least 15°. The `UPSILON_CMUP_CMX` trigger was simulated in the same way, but required fiduciality in CMX.

The p_T spectra of the Υ signals were generated using a gamma distribution with parameters fitted to the $\Upsilon(nS)$ differential cross section measurement made by CDF in Run I. Figure 18 shows

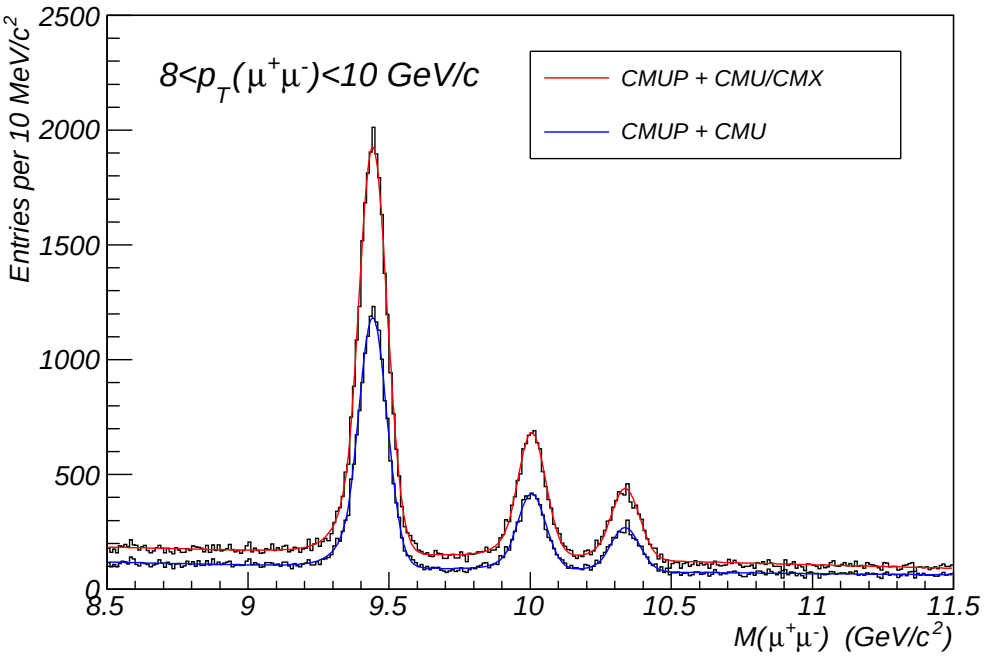

Figure 15: Example di-muon mass distribution from CDF data obtained with CMUP+CMU and CMUP+CMX triggers in the p_T range $8 < p_T(\mu^+\mu^-) < 10$ GeV/c. The signals are fit with a crystal ball function.

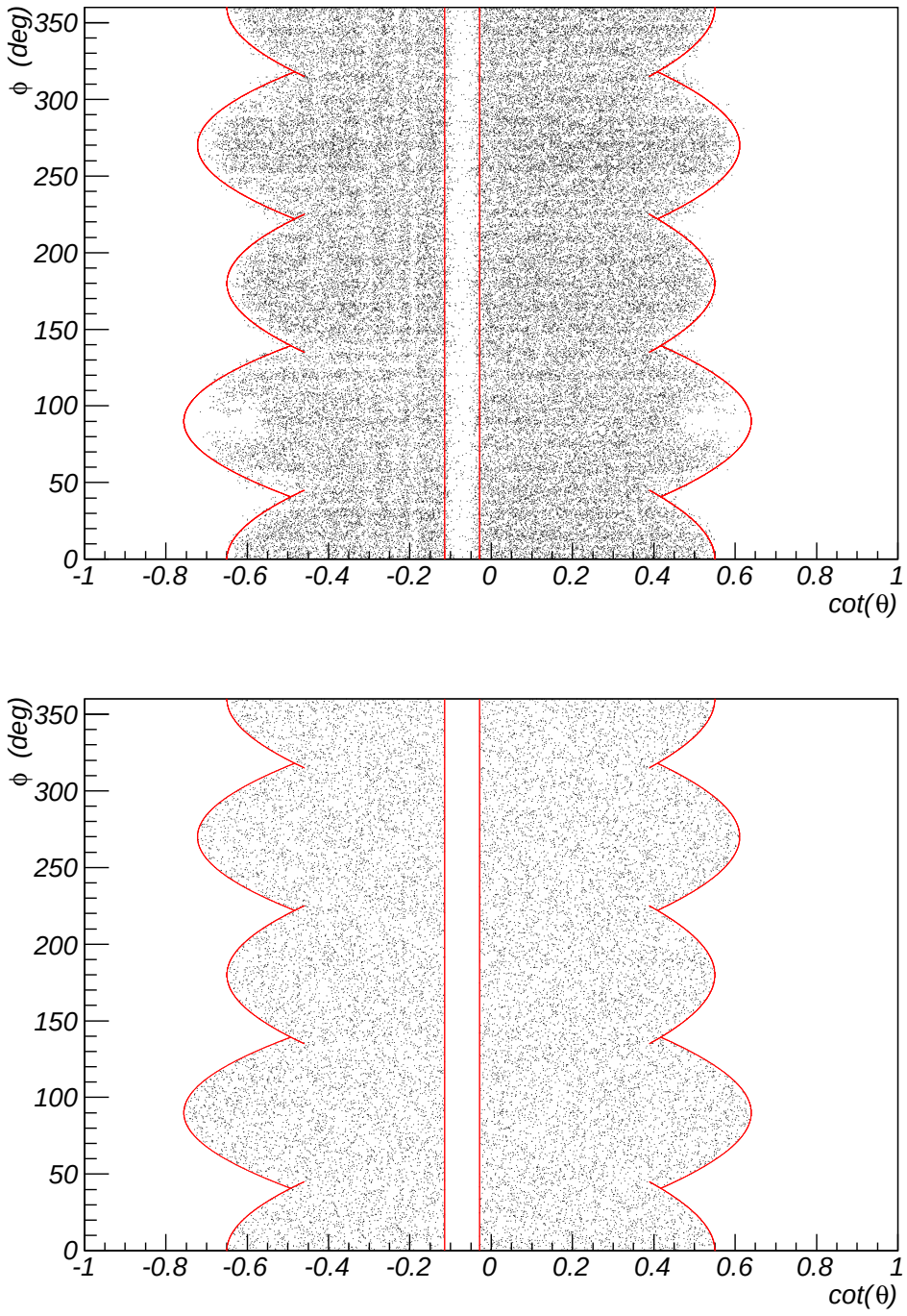

Figure 16: Observed (top) and simulated (bottom) acceptance for CMUP muons, selected to originate within 1 cm of $z_0 = 25$ cm.

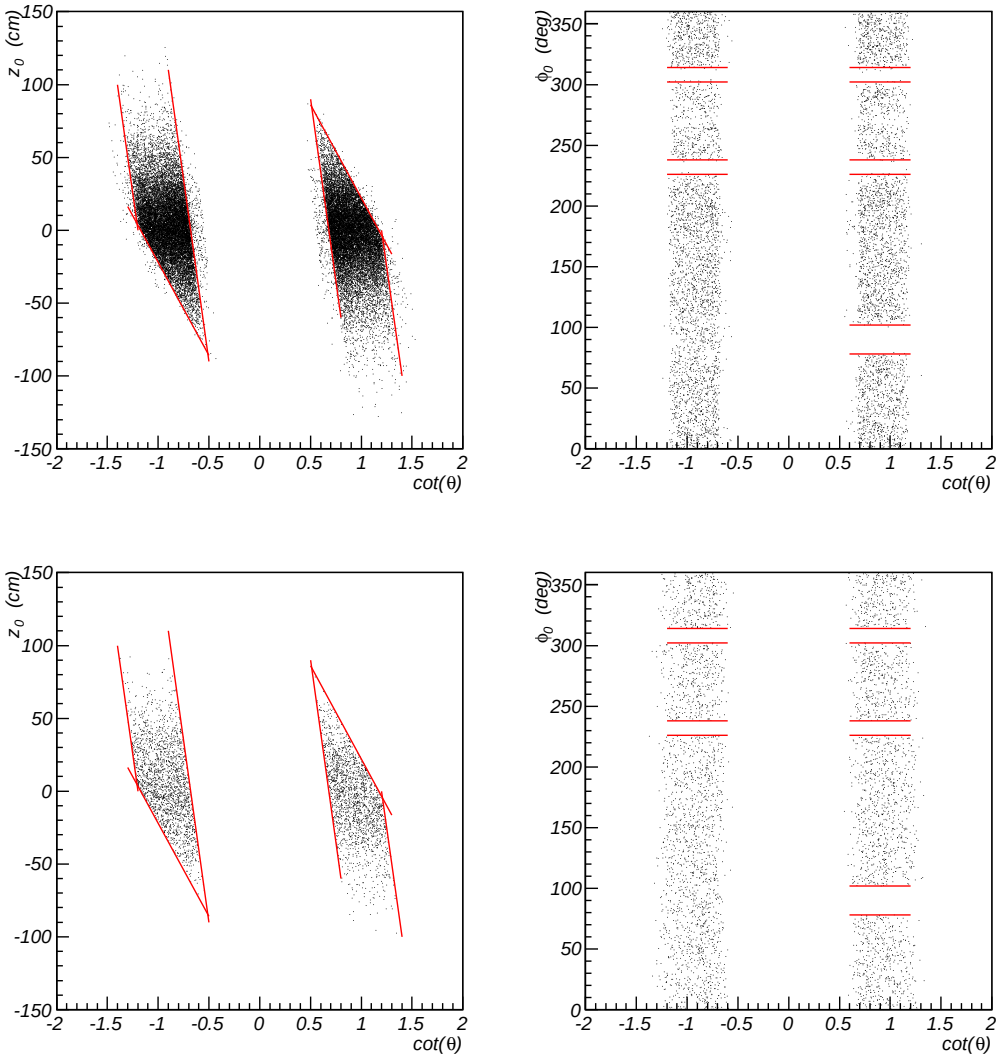

Figure 17: Observed (top) and simulated (bottom) acceptance for CMX muons.

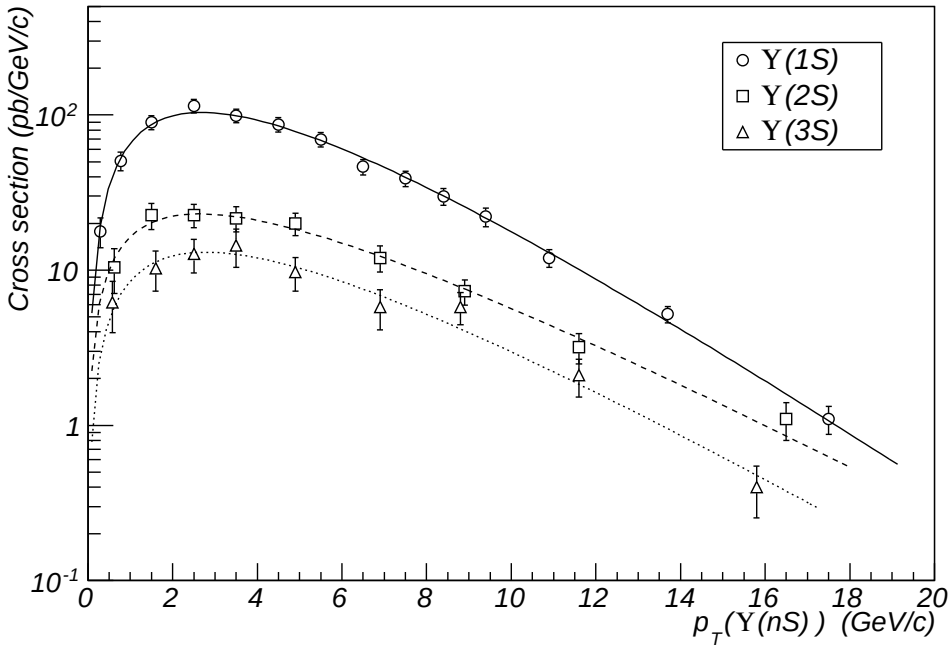

Figure 18: Differential cross section for $\Upsilon(nS)$ production from the Run I analysis fitted to gamma distributions. Only statistical uncertainties are shown.

State	γ	β [GeV/c]	χ^2/d.o.f.
$\Upsilon(1S)$	2.252 ± 0.062	2.131 ± 0.064	8.4/11
$\Upsilon(2S)$	1.96 ± 0.14	2.75 ± 0.23	3.8/6
$\Upsilon(3S)$	2.14 ± 0.23	2.43 ± 0.24	3.8/6

Table 2: Parameters in the gamma distribution used to fit the Run I Υ differential cross section data.

the Run I data with fits to the gamma function and Table 2 lists the parameters determined from the fits that are then used to generate the p_T spectrum in the toy Monte Carlo.

Table 3 lists the parameters used to generate the toy Monte Carlo signal samples. The sample sizes were chosen so as to reproduce the approximate signal yields, background levels and background shapes after the CMUP+CMU/CMX trigger simulation. Figure 19 shows a comparison of the reconstructed and simulated invariant mass distributions in the p_T range $8 < p_T(\mu^+\mu^-) < 10$ GeV/c.

5.1 Example analysis

Using the toy Monte Carlo samples generated with statistics equivalent to the event yields reconstructed in CDF data, we consider a hypothetical scenario in which the $\Upsilon(1S)$ is always in a pure transverse polarization state, but the orientation of the quantization axis rotates in the Collins-Soper frame as p_T increases. This is implemented by requiring $\tilde{\lambda} = +1$ and generating samples with $\lambda_\varphi = (1 - \lambda_\theta)/4$, with $-1/3 < \lambda_\theta < 1$. Figure 20 shows the evolution of the fitted 1σ contours in the $\lambda_\theta, \lambda_\varphi$ plane for this hypothetical experiment.

$p_T(\Upsilon)$ [GeV/c]	$N(1S)$	$N(2S)$	$N(3S)$	$N_{\rm bkg}$	σ [MeV/c^2]
0-2	120,000	30,000	15,000	300,000	46
2-4	700,000	150,000	70,000	1,500,000	46
4-6	700,000	180,000	90,000	1,800,000	47
6-8	380,000	110,000	58,000	1,000,000	47
8-10	220,000	70,000	40,000	450,000	47
10-12	120,000	40,000	22,000	220,000	48
12-15	75,000	30,000	20,000	75,000	57
15-20	45,000	17,000	11,000	68,000	62
20-50	15,000	7,000	5,000	30,000	68

Table 3: Generated $\Upsilon(nS)$ sample sizes, number of background events distributed between 8.5 and 11.5 GeV/c^2 and the signal mass resolution.

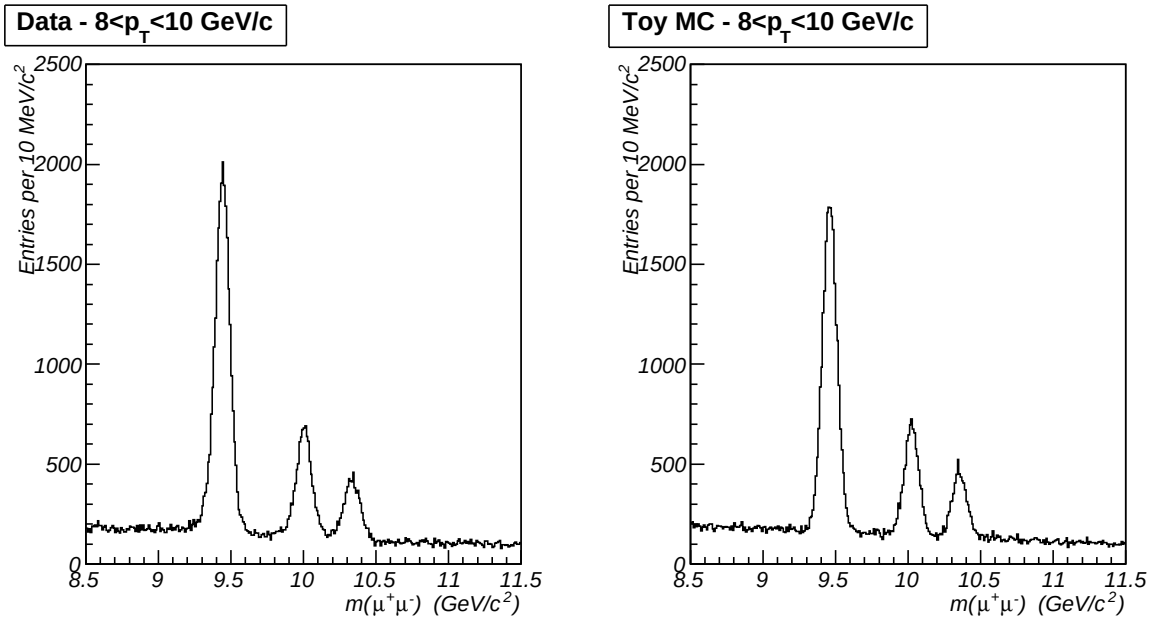

Figure 19: Comparison of reconstructed and simulated di-muon invariant mass spectra selected using the CMUP+CMU/CMX trigger paths.

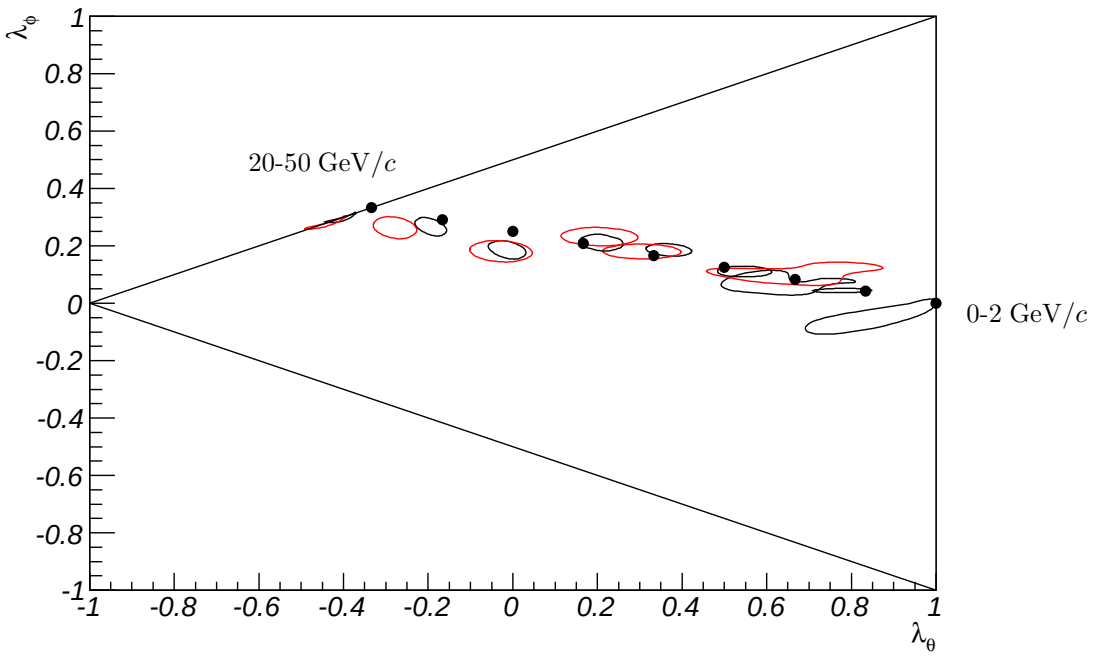

Figure 20: Fitted results from a hypothetical experiment in which the $\Upsilon(1S)$ is always in a pure transverse polarization state, but where the quantization axis rotates as a function of p_T. The red contours indicate the results obtained by restricting the sample to the CMUP+CMU trigger path. In that case, the fit did not converge for the three lowest p_T points.

6 Outlook

While this analysis provides polarization measurements on toy Monte Carlo samples, there are a number of changes that are needed in order to apply it to a data sample. Some of these issues are described below.

6.1 Monte Carlo samples

In general, it would be desirable to calculate the acceptance of the detector and trigger using the full detector simulation. Given that the average acceptance is about 10% for generation of events with $y| < 2$, it appears that suitable sample sizes would be approximately 100 times the size of the observed yields in data. The feasibility of maintaining samples this large remains to be determined.

6.2 Momentum spectrum of acceptance templates

The background and signal templates should have the same momentum spectrum as that observe in the data. This can be achieved either by re-weighting a flat distribution, or by iteratively generating samples with different distributions and iterating until the shape of the distribution after the acceptance cuts matches the data. It may also be necessary to assume a smooth function describing the evolution of the polarization parameters with p_T in order to determine yields accurately in small momentum slices.

6.3 Trigger efficiencies

The acceptance templates need to be re-weighted to account for the measured p_T dependent trigger efficiencies, or any other non-uniformity that is present in the data that is not included in the full or fast simulation. However, this fitting procedure lends itself well to accommodating such effects in this way.

6.4 Background description

The evolution of the background with invariant mass, both in yield and polarization, may be more complex than the linear functions considered here. However, with sufficient statistics in the side bands, it should be possible to compare the results with those obtained using higher order polynomials to describe these effects.

6.5 Angular distribution of background

The background might be more complex than the assumed spin-1 distributions considered here. Although we expect Drell-Yan processes to dominate, it may be necessary to examine the possibility of a spin-2 component in the background, at least as a cross check.

7 Summary

The fitter described in this note represents the first attempt at CDF to construct simultaneous estimates of the three polarization parameters in vector meson decays. It appears that we have already accumulated enough data to make meaningful measurements of the polarization as a function of p_T, which would be the first such measurement ever performed and may resolve some of the current experimental discrepancies.

After examining the extent of the information that we can obtain by analyzing vector meson decays using the full three dimensional angular distribution, it is worthwile reading further in Plato's *Allegory of the Cave*. The parallels between the allegory and the current state of experimental measurements are interesting, as are some of the outcomes that Plato explores.

Appendix A Helicity amplitude analysis

A.1 $\psi \to \mu^+\mu^-$ decay

A pure state describing a heavy vector meson can be written in terms of the basis states in which its spin is projected along a quantization axis:

$$|\psi\rangle = a_{-1}|1,-1\rangle + a_0|1,0\rangle + a_{+1}|1,+1\rangle \tag{14}$$

where the coefficients satisfy the normalization condition:

$$|a_{-1}|^2 + |a_0|^2 + |a_1|^2 = 1. \tag{15}$$

We wish to calculate the probability of observing a final state with particles oriented with angles θ, φ with respect to the quantization axis. That is, we wish to evaluate

$$|\overline{\mathcal{A}}(\theta,\varphi)|^2 \sim |\langle\theta\varphi|\psi\rangle|^2 \tag{16}$$

suitably summed over the unobserved spins of the final state particles.

The matrix representation of the rotation operator is defined

$$\mathcal{D}^j_{m'\,m}(\alpha,\beta,\gamma) = e^{-im'\alpha} d^j_{m'\,m}(\beta) e^{-im\gamma}. \tag{17}$$

For a spin-1 system, the Wigner little-d matrices can be expressed

$$d^1_{0,0}(\theta) = \cos\theta \tag{18}$$

$$d^1_{1,1}(\theta) = \frac{1+\cos\theta}{2} \tag{19}$$

$$d^1_{1,0}(\theta) = -\frac{\sin\theta}{\sqrt{2}} \tag{20}$$

$$d^1_{1,-1}(\theta) = \frac{1-\cos\theta}{2} \tag{21}$$

along with

$$d^j_{m'\,m}(\theta) = (-1)^{m'-m} d^j_{m\,m'}(\theta) = d^j_{-m\,-m'}(\theta). \tag{22}$$

The helicity amplitude for a pure state described by Equation 14 to make a transition to the $\mu^+\mu^-$ state is

$$\mathcal{A}_{\lambda_1\lambda_2}(\theta,\varphi) = \langle\theta\,\varphi;\lambda_1\lambda_2|\psi\rangle \tag{23}$$

$$= \sqrt{\frac{3}{4\pi}} A_{\lambda_1\lambda_2}\left(a_{-1}\mathcal{D}^1_{-1\lambda}(\varphi,\theta,-\varphi)^* + a_0\mathcal{D}^1_{0\lambda}(\varphi,\theta,-\varphi)^* + a_{+1}\mathcal{D}^1_{1\lambda}(\varphi,\theta,-\varphi)^*\right) \tag{24}$$

where $\lambda = \lambda_1 - \lambda_2$. From parity conservation, $A_{-\frac{1}{2}\,\frac{1}{2}} = A_{\frac{1}{2},-\frac{1}{2}}$ and $A_{\frac{1}{2}\,\frac{1}{2}} = A_{-\frac{1}{2}\,-\frac{1}{2}} = 0$ because the ψ decay does not couple strongly to final states in which both muons have equal helicity. Thus, the angular distribution is obtained by squaring this amplitude and summing over the two possible helicity combinations of the final state:

$$\begin{aligned}|\overline{\mathcal{A}}(\theta,\varphi)|^2 = \frac{3|A_{-\frac{1}{2}\,\frac{1}{2}}|^2}{8\pi}\Big(&1 + |a_0|^2 + (1-3|a_0|^2)\cos^2\theta + 2\mathrm{Re}\left(a^*_{+1}a_{-1}\right)\sin^2\theta\cos 2\varphi + \\ &\sqrt{2}\mathrm{Re}\left(a^*_0(a_{+1}-a_{-1})\sin 2\theta\cos\varphi + 2\mathrm{Im}\left(a^*_{+1}a_{-1}\right)\sin^2\theta\sin 2\varphi + \right. \\ &\left.-\sqrt{2}\mathrm{Im}\left(a^*_0(a_{+1}+a_{-1})\right)\sin 2\theta\sin\varphi\Big)\end{aligned} \tag{25}$$

which can be more conveniently written

$$|\overline{\mathcal{A}}(\theta,\varphi)|^2 = \frac{3|A_{-\frac{1}{2}\,\frac{1}{2}}|^2}{8\pi}\left(1+|a_0|^2\right)\Big(1+\lambda_\theta\cos^2\theta+\lambda_\varphi\sin^2\theta\cos 2\varphi+\lambda_{\theta\varphi}\sin 2\theta\cos\varphi+ \lambda_\varphi^\perp\sin^2\theta\sin 2\varphi+\lambda_{\theta\varphi}^\perp\sin 2\theta\sin\varphi\Big) \quad (26)$$

where

$$\lambda_\theta = \frac{1-3|a_0|^2}{1+|a_0|^2} \quad (27)$$

$$\lambda_\varphi = \frac{2\mathrm{Re}\left(a_{+1}^* a_{-1}\right)}{1+|a_0|^2} \quad (28)$$

$$\lambda_{\theta\varphi} = \frac{\sqrt{2}\mathrm{Re}\left(a_0^*(a_{+1}-a_{-1})\right)}{1+|a_0|^2} \quad (29)$$

$$\lambda_\varphi^\perp = \frac{2\mathrm{Im}\left(a_{+1}^* a_{-1}\right)}{1+|a_0|^2} \quad (30)$$

$$\lambda_{\theta\varphi}^\perp = -\frac{\sqrt{2}\mathrm{Im}\left(a_0^*(a_{+1}+a_{-1})\right)}{1+|a_0|^2} \quad (31)$$

Consider the special cases where $a_{+1}=1$ and $a_0=a_{-1}=0$, or where $a_{+1}=a_0=0$ and $a_{-1}=1$ which arise when $\hat{\theta}=0$ or π and $\hat{\phi}=0$. In such a case, $\lambda_\theta=1$, $\lambda_\varphi=0$, $\lambda_{\theta\varphi}=0$, $\lambda_\varphi^\perp=0$ and $\lambda_{\theta\varphi}^\perp=0$, which gives

$$|\overline{\mathcal{A}}_{\pm 1}(\theta,\varphi)|^2 = \frac{3|A_{-\frac{1}{2}\,\frac{1}{2}}|^2}{8\pi}\Big(1+\cos^2\theta\Big). \quad (32)$$

such that

$$\int |\overline{\mathcal{A}}_{\pm 1}(\theta,\varphi)|^2 d\Omega = 2|A_{-\frac{1}{2}\,\frac{1}{2}}|^2. \quad (33)$$

Similarly, when $a_{+1}=a_{-1}=0$ and $a_0=1$, we have $\lambda_\theta=-1$ with all other coefficients vanishing. In this case,

$$|\overline{\mathcal{A}}_0(\theta,\varphi)|^2 = \frac{3|A_{-\frac{1}{2}\,\frac{1}{2}}|^2}{4\pi}\Big(1-\cos^2\theta\Big). \quad (34)$$

so that again we find:

$$\int |\overline{\mathcal{A}}_0(\theta,\varphi)|^2 d\Omega = 2|A_{-\frac{1}{2}\,\frac{1}{2}}|^2. \quad (35)$$

If, however, the initial state is not a pure state, then we must sum over its composite pure states weighted by their relative probabilities. If the initial state had equal probability of being in each of the basis states then the resulting angular distribution would be of the form shown in Equation 26 but with coefficients given by $\lambda_\theta = 1-2+1=0$, $\lambda_\varphi=\lambda_{\theta\varphi}=\lambda_\varphi^\perp=\lambda_{\theta\varphi}^\perp=0$ and the resulting angular distribution is isotropic, as expected.

A.2 Symmetry properties

The angular distribution shown in Equation 26 has symmetry properties that can be exploited in an analysis. In particular the first three terms in the distribution are symmetric under the transformation $(\theta,\varphi)\to(\theta,-\varphi)$ as well as $(\theta,\varphi)\to(\pi-\theta,\pi-\varphi)$, while the terms with coefficients $\lambda_\varphi^\perp$ and $\lambda_{\theta\varphi}^\perp$ are antisymmetric.

A.3 Physical bounds on λ_θ, λ_φ and $\lambda_{\theta\varphi}$

Consider a pure transverse state $|\psi_T\rangle$ in which $a_{+1} = 1$ and $a_0 = a_{-1} = 0$. A general rotation can be represented by

$$\mathcal{R}(\theta,\phi) = \begin{pmatrix} \frac{1}{2}(1+\cos\theta)e^{-i\phi} & -\frac{\sin\theta}{\sqrt{2}}e^{-i\phi} & \frac{1}{2}(1-\cos\theta)e^{-i\phi} \\ \frac{\sin\theta}{\sqrt{2}} & \cos\theta & -\frac{\sin\theta}{\sqrt{2}} \\ \frac{1}{2}(1-\cos\theta)e^{i\phi} & \frac{\sin\theta}{\sqrt{2}}e^{i\phi} & \frac{1}{2}(1+\cos\theta)e^{i\phi} \end{pmatrix} \tag{36}$$

and will transform the state into $|\psi'_T\rangle = a'_{+1}|1,+1\rangle + a'_0|1,0\rangle + a'_{-1}|1,-1\rangle$ where

$$a'_{+1} = \frac{1+\cos\theta}{2}e^{-i\phi} \tag{37}$$

$$a'_0 = -\frac{\sin\theta}{\sqrt{2}} \tag{38}$$

$$a'_{-1} = \frac{1-\cos\theta}{2}e^{i\phi}. \tag{39}$$

and the polarization parameters will depend on θ and ϕ as follows:

$$\lambda_\theta^T(\theta,\phi) = \frac{2-3\sin^2\theta}{2+\sin^2\theta} \tag{40}$$

$$\lambda_\varphi^T(\theta,\phi) = \frac{\sin^2\theta\cos 2\phi}{2+\sin^2\theta} \tag{41}$$

$$\lambda_{\theta\varphi}^T(\theta,\phi) = -\frac{2\sin\theta\cos\theta\cos\phi}{2+\sin^2\theta} \tag{42}$$

In this case, $\lambda_\varphi^T(\theta,\phi)$ can be expressed in terms of $\lambda_\theta^T(\theta,\phi)$:

$$\lambda_\varphi^T(\theta,\phi) = \frac{1}{4}\left(1-\lambda_\theta^T(\theta,\phi)\right)\cos 2\phi \tag{43}$$

and the allowed values for $\lambda_\varphi^T(\theta,\phi)$ lie between $\pm\frac{1}{4}\left(1-\lambda_\theta^T(\theta,\phi)\right)$. Thus, when $\lambda_\theta^T = -1$, $\lambda_\varphi^T \in (-\frac{1}{2},+\frac{1}{2})$ while when $\lambda_\theta^T = +1$, λ_φ^T is constrained to be zero.

Similarly, a purely longitudinal state, $|\psi_L\rangle$ with $a_0 = 1$ and $a_{\pm1} = 0$ will be transformed into a state $|\psi'_L\rangle = a''_{+1}|1,+1\rangle + a''_0|1,0\rangle + a''_{-1}|1,-1\rangle$ where

$$a''_{+1} = -\frac{\sin\theta}{\sqrt{2}}e^{-i\phi} \tag{44}$$

$$a''_0 = \cos\theta \tag{45}$$

$$a''_{-1} = \frac{\sin\theta}{\sqrt{2}}e^{i\phi}. \tag{46}$$

which gives

$$\lambda_\theta^L(\theta,\phi) = -\frac{2-3\sin^2\theta}{2-\sin^2\theta} \tag{47}$$

$$\lambda_\varphi^L(\theta,\phi) = -\frac{\sin^2\theta\cos 2\phi}{2-\sin^2\theta} \tag{48}$$

$$\lambda_{\theta\varphi}^L(\theta,\phi) = -\frac{2\sin\theta\cos\theta\cos\phi}{2-\sin^2\theta} \tag{49}$$

and $\lambda_\varphi^L(\theta,\phi)$ can be written in terms of $\lambda_\theta^L(\theta,\phi)$ thus:

$$\lambda_\varphi^L(\theta,\phi) = -\frac{1}{2}\left(1+\lambda_\theta^L(\theta,\phi)\right)\cos 2\phi \tag{50}$$

Therefore, $\lambda_{\varphi}^{L}(\theta,\phi)$ is always constrained to lie between $\pm\frac{1}{2}(1+\lambda_{\theta}^{L}(\theta,\phi)$. When $\lambda_{\theta}^{L}(\theta,\phi)=1$, $\lambda_{\varphi}^{L}(\theta,\phi)\in(-1,1)$. While when $\lambda_{\theta}^{L}(\theta,\phi)=-1$, $\lambda_{\varphi}^{L}(\theta,\phi)=0$.

Note that further constraints restrict the allowed range of $\lambda_{\theta\varphi}$. In general, however, the relations are quite complicated.

References

[1] Plato, *The Republic*, Book VII.

[2] D. Acosta *et al.* (CDF Collaboration), Υ *Production and Polarization in* $p\overline{p}$ *Collisions at* $\sqrt{s}=$ 1.8 TeV, Phys. Rev. Lett. 88, 161802 (2002).

[3] V.M. Abazov *et al.* (DØCollaboration), *Measurement of the Polarization of the* $\Upsilon(1S)$ *and* $\Upsilon(2S)$ *States in* $p\overline{p}$ *Collisions at* $\sqrt{s}=1.96$ TeV, Phys. Rev. Lett. 101, 182004 (2008).

[4] M. Jones, *Almost Exact Statistical Formulæfor Signal Yield Estimates*, CDF Note 10387, January 25, 2011.